

An Investigation of Chemo-Mechanical Phenomena and Li Metal Penetration in All-Solid-State Lithium Metal Batteries Using In Situ Optical Curvature Measurements

Jung Hwi Cho, Kunjoong Kim, Srinath Chakravarthy, Xingcheng Xiao, Jennifer L. M. Rupp, and Brian W. Sheldon*

Solid-electrolytes (SEs) can provide a pathway to increase energy-density in lithium metal batteries. However, lithium metal penetration through garnet based LLZO solid electrolytes has been identified as a critical failure process. This phenomenon is related to chemo-mechanical processes which are difficult to probe. In particular, characterizing the dynamic mechanical deformations that occur in electrode-SE structures is very challenging. This study reports in situ curvature measurements that are thus designed to probe chemo-mechanical phenomena that occur during lithium plating. The novel experimental cell configuration created for this work shows that pressure builds up in the Li metal during plating, up until the point where short circuits occur. The resulting data are analyzed with a detailed finite element model (FEM) to quantitatively evaluate stress evolution. The results show that Li metal plating within a surface flaw can produce stress build-up prior to short-circuiting. The combined results from both the experiments and the FEM suggest that it is critical to minimize surface defects and flaws during the manufacturing processes.

1. Introduction

Solid electrolytes (SEs) are a promising replacement for the liquid electrolytes that are commonly used in Li ion batteries. LLZO, nominal composition $\text{Li}_7\text{La}_3\text{Zr}_2\text{O}_{12}$, is a leading candidate which exhibits high ionic conductivities, however, lithium metal penetration through LLZO SEs has been identified as a critical failure process.^[1] At a critical current density (CCD), LLZO can short-circuit via a process that appears to fracture the SE.^[2–8] Chemical modifications at the interfaces such as dopants and coatings can improve performance.^[9–15] However, chemo-mechanical phenomena are accentuated at SE-electrode interfaces, and the impact of these effects on all solid-state batteries has been addressed and emphasized only recently.^[1,4,5,7,8,16–23]

Some recent studies of LLZO have proposed that the Li flux during plating can create significant stresses in surface flaws and/or porosity.^[4–8,18,24–30] **Figure 1** shows a schematic of this type of process, where current focusing near the tip accentuates stress build up inside of a surface flaw. A second, related hypothesis is that these stresses are large enough to fracture a SE, and that this is an important mechanism that leads to short circuits via Li metal penetration. These hypotheses are currently controversial, largely because bulk lithium metal has a very low yield stress (<1 MPa) which should alleviate the stress build-up in the SE.^[18,31,32] The plastic deformation of lithium metal and the tractions within the flaw may affect stresses in a flaw. For example, some recent models assume that Li behavior resembles a viscous fluid and that it will thus readily flow out of a surface flaw after a significant increase in compressive stress near the tip,^[6,18,29] whereas another modeling effort argues that stress relaxation due to this type of flow will be limited by deformation behavior of the underlying bulk Li slab.^[26] The assumptions in these models lead to very different conclusions about the impact of internal stresses, and the operative mechanisms under different condition are still in question. The possible mechanisms and material properties that are potentially related to Li penetration in LLZO due to the effects of a surface crack or flaw are outlined in Figure 1.

J. H. Cho, B. W. Sheldon
School of Engineering
Brown University
Providence, RI 02912, USA
E-mail: brian_sheldon@brown.edu

K. Kim, J. L. M. Rupp
Department of Materials Science and Engineering
Massachusetts Institute of Technology
Cambridge, MA 02139, USA

S. Chakravarthy
Advanced Materials Lab
Samsung Semiconductor, Inc.
Cambridge, MA 02138, USA

X. Xiao
Chemical and Materials Systems Lab
General Motors Research and Development Center
Warren, MI 48092, USA

J. L. M. Rupp
Department of Electrical Engineering and Computer Science
Massachusetts Institute of Technology
Cambridge, MA 02139, USA

 The ORCID identification number(s) for the author(s) of this article can be found under <https://doi.org/10.1002/aenm.202200369>.

DOI: 10.1002/aenm.202200369

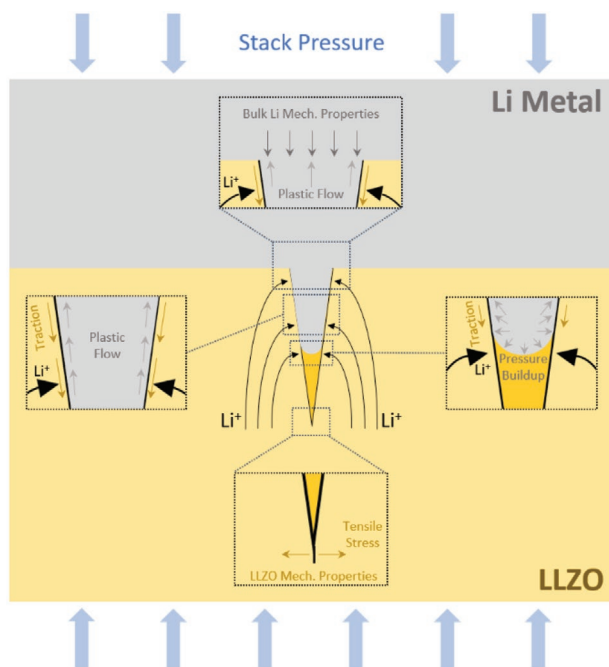


Figure 1. Schematic showing possible mechanical mechanisms associated with electrochemical plating in a surface crack/flaw of a ceramic electrolyte. Due to the geometry of the Li/LLZO interface inside of the flaw, current redistribution results in additional lithium plating inside the surface flaw. The electrochemically-induced volume expansion that occurs here leads to pressure buildup in the metal. Relaxation of this compressive stress depends on the electrochemical conditions, the dimensions of the flaw, and mechanical properties of both lithium metal and LLZO (e.g., Li metal plasticity, LLZO fracture toughness, etc.). Mechanical deformation can also be influenced by external forces associated with the battery configuration, such as the stack pressure.

While chemo-mechanical phenomena during electrochemical cycling with ceramic electrolytes have been widely discussed, it is generally very difficult to directly investigate the stresses that evolve inside of these materials. To address this, a novel experimental configuration is employed to permit in situ bending measurements during lithium plating. The technique

established here contrasts to prior art in the field where the evolution of Li-dendrites is typically probed by either optical microscopy,^[6,8] X-ray tomography,^[33,34] or neutron depth profiling.^[35,36] These methods make it possible to image Li metal penetration, but they do not provide direct information about mechanical deformation during electrochemical cycling. In contrast, in situ wafer curvature measurements can be used to carefully monitor the displacements that are caused by mechanical forces which arise during electrochemical cycling. The specific method employed in this study employs multiple parallel laser beams (roughly 1.7 mm apart) that reflect off of the current collector, providing curvature resolution up to 0.00002 m^{-1} .^[37] The in situ curvature values are then obtained from the spacing between adjacent beams (detected in a CCD detector). Applying this method to a solid state battery differs considerably from the conventional implementation of wafer curvature to measure in-plane biaxial stress in thin films. For the current work, we modify the measurement geometries by employing a highly reflective current collector that makes it possible to probe the expansion of a Li metal electrode on LLZO material. This method can also be expanded further to explore a wider range of experimental configurations. Interpretation of the measurements is based on an approximate analytical approach, and a detailed finite element model (FEM) that describes both electrochemical processes and the mechanical response due to lithium plating. Collectively, these results contribute to an understanding of lithium plating through an LLZO SE.

2. Results

2.1. Mechanical Deformation and Lithium Penetration

The configuration in **Figure 2** was initially used to measure curvature evolution during Li plating through the LLZO SE. Here, the current collector layers (50 nm Au and 1 μm Cu) were deposited on the LLZO. The thin Au layer here acts as a seed layer that enables more uniform Li metal plating. Because Li alloys significantly with Au, this was capped with a thicker 1 μm Cu current collector. These metal layers were then capped with

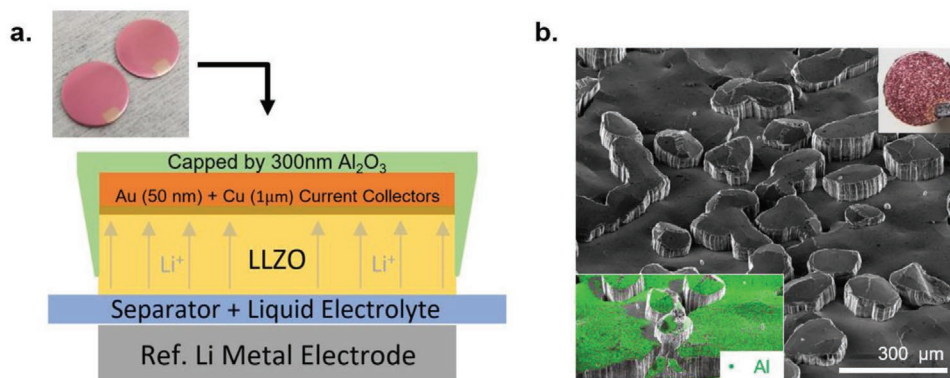


Figure 2. a) Schematic of the initial specimen in a half-cell as one of the first attempts for this study. The optical image shown is the resulting sample after the alumina capping. Small portion of the top surface of the samples is the exposed copper current collector for electrical connection. b) SEM image of the roughened sample (optical image shown in the top-right inset) after plating. The EDS signature of aluminum in the lower left inset corresponds to the Al₂O₃ capping layer showing protrusions caused by the internal pressure buildup of lithium during plating.

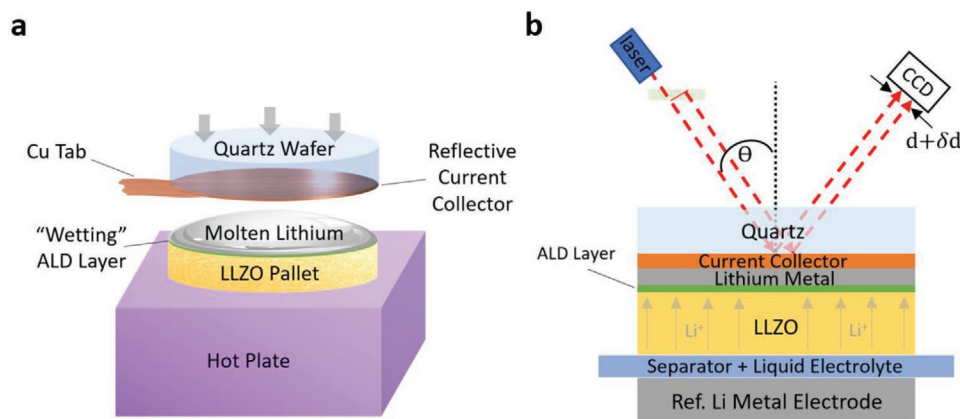


Figure 3. a) Schematic of the improved design of the half-cell used for in situ curvature measurements in this study. Each specimen was prepared by bonding a reflective/current-collecting quartz glass wafer and the LLZO pellet with molten lithium metal. The contact between LLZO and the molten lithium metal was improved by applying a thin layer of Al_2O_3 via atomic layer deposition method. b) Schematic showing how the curvature evolution is measured during plating using the cell design in Figure 2a. During the measurement, a set of parallel laser beams are reflected off the reflecting current collector, which tracks the evolving curvature associated within lithium metal during plating.

300 nm of aluminum oxide in an initial attempt to mechanically confine the growing Li metal during plating (see Figure 3b). The physical vapor deposition methods used for these films produce a reflective surface (see Figure 2a) for the optical measurements. However, the surface roughened significantly after a moderate amount of lithium plating (average thickness of $\approx 10 \mu\text{m}$), and this disrupted the optical measurements. The SEM image in Figure 2b shows that lithium columns protruding through the Al_2O_3 layer caused the loss of reflectivity. This observation of soft lithium metal columns that can push through a high modulus alumina layer indicates that there is a significant internal pressure buildup in the lithium metal during plating.

In subsequent experiments, the same custom $\text{Li}|\text{LLZO}|\text{Li}$ symmetric cell was employed, however, a $500 \mu\text{m}$ thick quartz wafer was used to constrain the internal pressure build up caused by plating of lithium metal. The configuration is illustrated in Figure 3. Here, a reflective/current-collecting metal film on a quartz glass wafer was bonded to the Al_2O_3 -ALD-coated LLZO pellet with molten lithium metal as shown in Figure 3a. The curvature was then tracked during lithium plating with a set of parallel laser beams that reflect off the current collector. The other side of the LLZO was placed in a liquid electrolyte and a separator was placed between the pellet and the reference lithium metal counter electrode. This allows the full multilayer specimen to bend during electrochemical cycling. The cell preparation details are described further in the Experimental Section. For the initial experiments, galvanostatic plating was conducted with an initial current density of 0.01 mA cm^{-2} , followed by stepwise increases of 0.01 mA cm^{-2} every 12 h until short-circuiting. The current was always unidirectional (i.e., there was no stripping sequence). The critical current density for all specimens ranged from $0.03\text{--}0.06 \text{ mA cm}^{-2}$, which is comparable to other reports of “natural critical current densities,” where little to no external stack pressure was applied.^[38–41] Results for this type of experiment are shown in Figure 4, where a large increase in curvature occurs prior to the large voltage drop that signals a short-circuit.

At this point the curvature increase was also interrupted. Other experiments showed a similar curvature increase prior to the short-circuit (see Figure S1, Supporting Information). A sharp change in curvature was always observed after the short-circuit, but the curvature decrease in Figure S1b was only observed in some cases, while in other experiments the curvature was relatively constant after the short circuit (e.g., Figure 4). The large curvature increases during plating indicate that non-uniform stress evolves in the underlying multilayer structure. This is related to deformation of the lithium metal since our experiment tracks bending at the current collector film that is directly bonded to this layer. Contributions due to stresses that occur in the LLZO should also impact the curvature via changes in the Li layer. The possible causes of the observed bending are elucidated further below with both analytical and FEM based descriptions.

After the experiment the cell was disassembled in an Argon filled glovebox. The post-mortem optical image in Figure 4b shows that the shorted pellets exhibit a main crack-like feature that propagates through the LLZO. Figure 4c,d indicates that the fracture surface along the Li metal penetration line shows a web-like network that some researchers have attributed to penetration along LLZO grain boundaries (GBs).^[2,3,15,30] This type of penetration was observed in all shorted pellets, and it was not observed in any other locations (i.e., it occurred only along the apparent short-circuit line shown in Figure 4b). The network seen here consists of isolated LLZO regions that are significantly larger than the average grain size of $2.38 \mu\text{m}$ shown in Figure S9, Supporting Information, which indicates that Li only penetrates along some of the GBs. The “web-like” structures defined by the Li are $\approx 44 \mu\text{m}$ and $\approx 32 \mu\text{m}$ wide near the plating and separator side, respectively. It is also clear that these “webs” differ in density and size between both interfaces and are largest close to the plating side of the LLZO. Further evidence of the difference across the material is seen in the width of the Li features, which varies across the SE, from $\approx 4 \mu\text{m}$ near the plating side to $\approx 2.5 \mu\text{m}$ near the separator (in the images these features correspond to Li that extends beyond the grain surfaces,

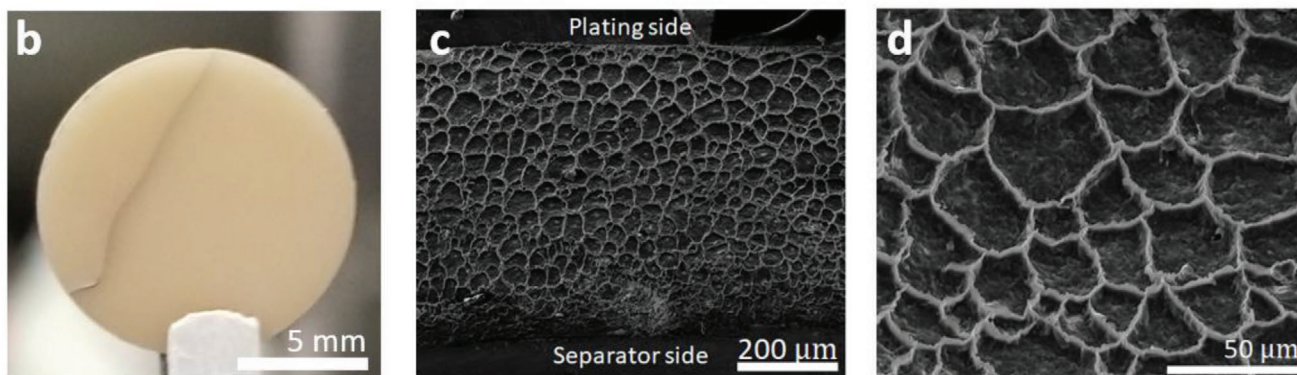
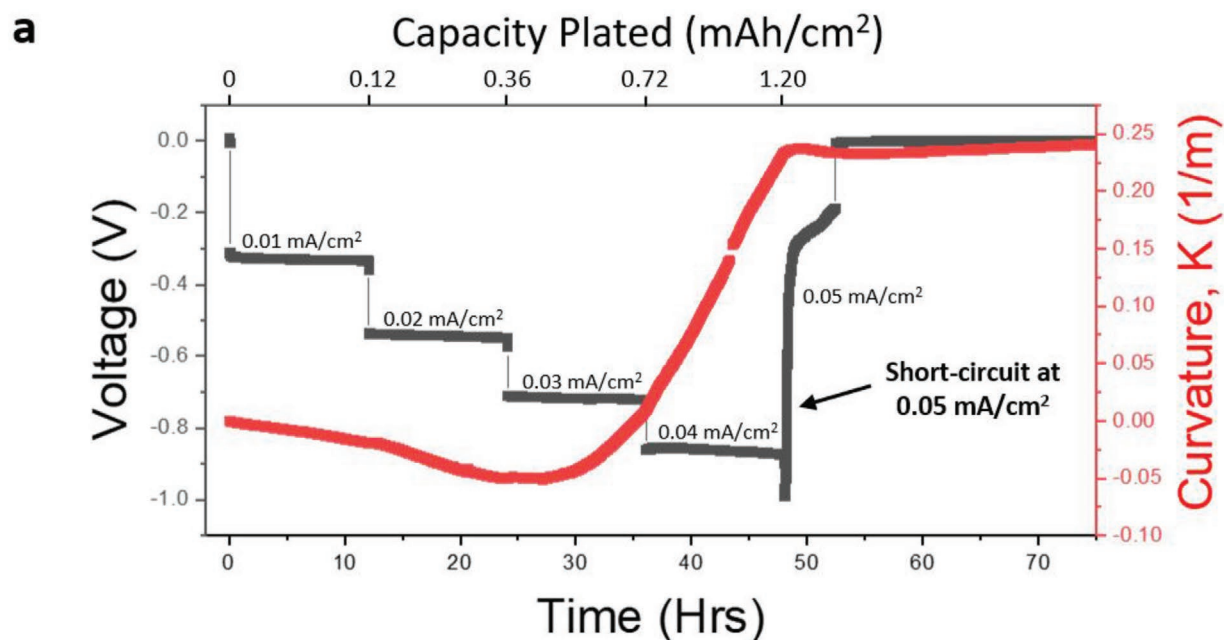


Figure 4. a) Voltage & curvature versus time & capacity plated of the LLZO/quartz electrode. Black and red lines indicate voltage and curvature profile, respectively. Plating current is applied as a stepwise increase of 0.01 mA cm^{-2} increments every 12 h, starting at 0.01 mA cm^{-2} . b) Visible crack and fracture on the LLZO pellet after the shorting experiment. c,d) Cross-sectional SEM image of the fracture surface after manually breaking the pellet along the crack.

and thus the apparent dimensions are significantly larger than the actual GB widths). The differences in the Li network structure across the SE appear to be associated with unidirectional plating, since these variations have not been reported in previous work where cycling was conducted in both directions.^[2,3,15]

2.2. Steady-State Curvature with Extended Plating at Low Current Densities

The abrupt change in the curvature trajectory after short circuits and the post-mortem images indicate that Li metal penetration through the SE is accompanied by changes in the stress distribution in the Li layer. This was examined further with the experiments summarized in **Figure 5**. After initial galvanostatic plating at 0.01 mA cm^{-2} for 12 h, longer times were employed at higher current densities of 0.02 and 0.03 mA cm^{-2} . These relatively low currents reduce the likelihood of shorting,

and the measurements show that the curvature increase eventually stops after a significant amount of plating occurs at these lower currents. At these longer times the curvature reaches an approximate plateau where additional changes are relatively small. This indicates that after sufficiently long times, the stress distribution in the lithium reaches a steady-state of some kind (i.e., where stress build-up no longer occurs, even though lithium is still plating). In **Figure 5a** the higher plateau reached when the current density is increased from 0.02 to 0.03 mA cm^{-2} also indicates that this steady-state is a function of the applied current. In **Figure 5b**, a longer hold at this current density also shows a gradual decrease in curvature at longer times, which coincides with a slow decrease in the voltage at 0.03 mA cm^{-2} ($\approx 50 \text{ h}$) prior to short-circuiting. This observation is consistent with recent observations, which suggest that a decrease in overpotential can occur prior to short-circuiting. This may be correlated with increased lithium plating inside of the filaments that penetrate into the electrolyte.^[6,8,33]

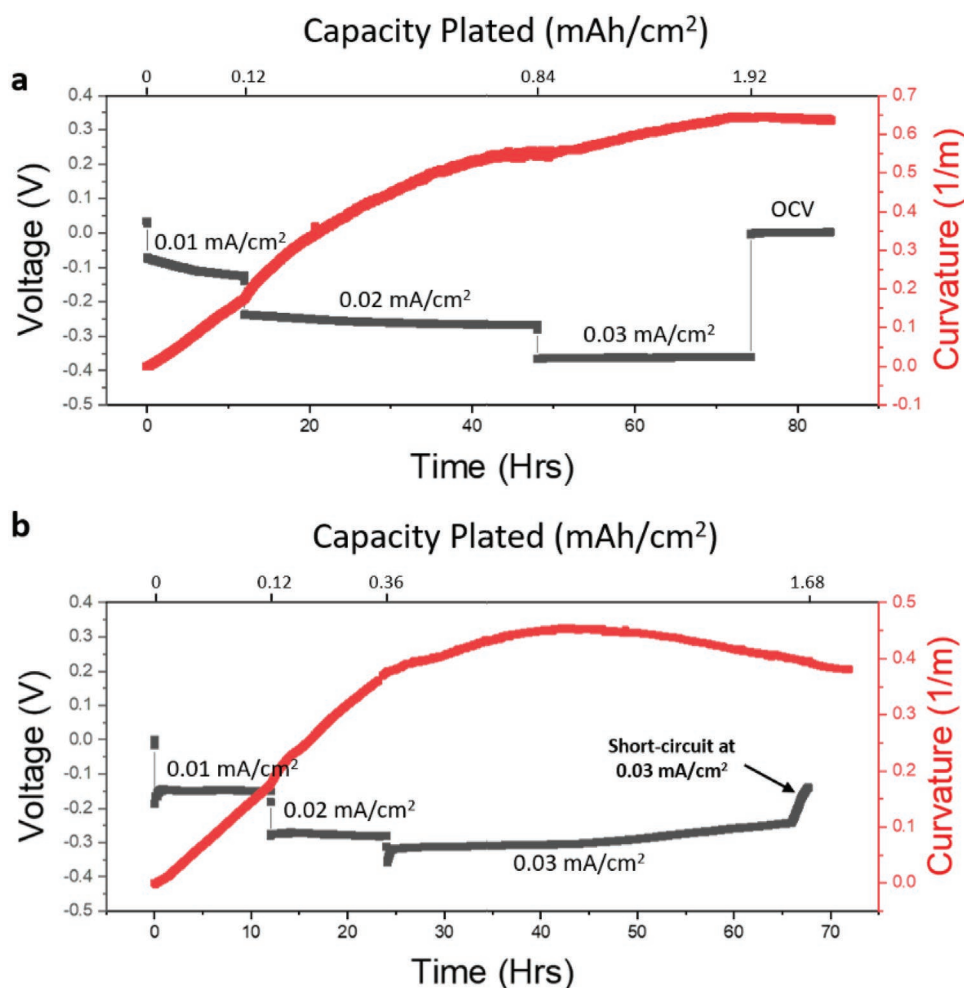


Figure 5. a) Voltage & curvature versus time & capacity plated of the LLZO/quartz electrode with extended plating time. Black and red lines indicate voltage and curvature profile, respectively. Curvature reaches a steady-state after an extended time of plating at current densities below its CCD. The results shown in Figure 4a indicate that the steady-state curvature associated with evolving plated lithium metal is a function of current density. b) Similar experiment with extended plating time as shown in Figure 4a. Here, a decrease in overpotential shows correlation with decrease in curvature after reaching a steady-state, followed by a short-circuit event.

In general, curvature plateaus only occurred after a significant amount of lithium plating at relatively low current densities. The long times that it takes to reach these plateaus imply that the continuously increasing curvatures during shorter galvanostatic holds (e.g., in Figure 4a) occur because the deformation in the Li metal has not yet reached steady-state. Thus the results in Figure 4 imply that stresses in these structures evolve continuously during plating, unless sufficiently long times are employed. The rate of change (i.e., slope) of the curvature is directly related to the slow evolution of the stress distribution in the lithium metal layer. Quantitative analysis of these slopes will require improvements in the experimental configuration. An example of the inherent complexity involved is seen in Figure 5a, where the curvature increases faster at lower current (0.02 mA cm^{-2}) than it does at higher current (0.03 mA cm^{-2}). A key difference is that the lower current is applied relatively early in the experiment, before a plateau has been reached. Thus, the slope reflects an evolving stress distribution due to both the increased current and the initial plating at lower current, where

the pressure has not yet stabilized. Similar transients in the curvature are also seen in the experiments with shorter current holds (Figure 6a and Figure S1a, Supporting Information). In contrast, the increase to 0.03 mA cm^{-2} occurs after the curvature reaches a steady-state plateau, at which point the transients from plating at lower currents have largely dissipated.

2.3. Partial Lithium Metal Penetration

The correlations between curvature evolution and lithium penetration were explored further with post-mortem characterization of specimens where plating was terminated after the onset of significant stress-build up, but prior to short-circuiting. Figures 6 and 7 show results where the galvanostatic steps resemble those in Figure 4, except that OCV holds were inserted to determine if the stress continued to evolve after plating was halted. The electrochemical data show that increased curvature is correlated with changes in the voltage,

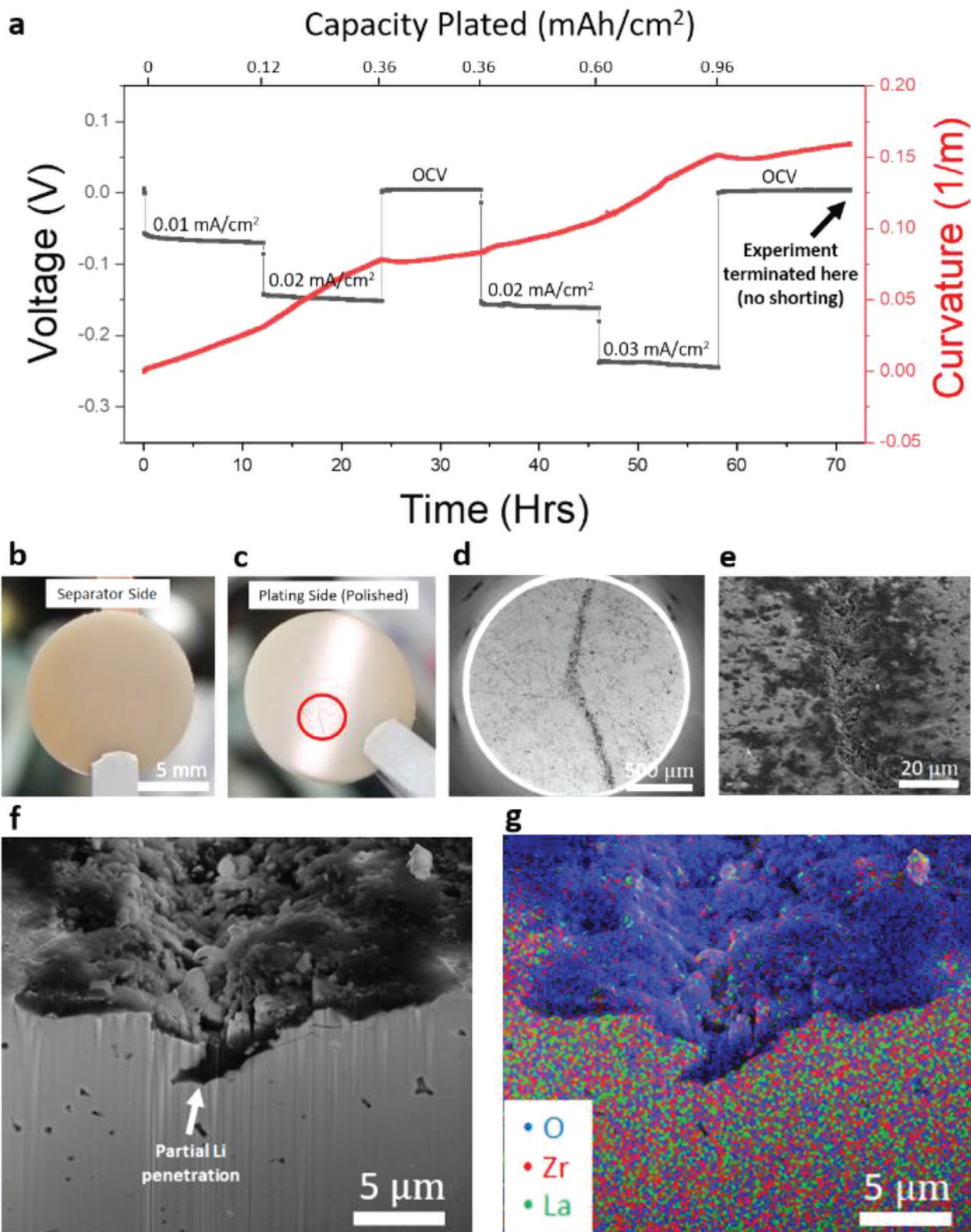


Figure 6. a) Voltage & curvature versus time of the LLZO/quartz electrode. Black and red lines indicate voltage and curvature profile, respectively. b,c) Separator and plating side of the LLZO pellet after the experiment shown in Figure 5a. On the plating side, a small crack is observed after lightly polishing and removing the residual lithium metal. d,e) observed crack in the SEM. f) FIB cut on the crack reveals a partial lithium metal penetration through the solid electrolyte. g) EDS mapping of the FIB cut cross-section. Blue, red, and green dots indicate signatures of Oxygen, Zirconium, and Lanthanum, respectively.

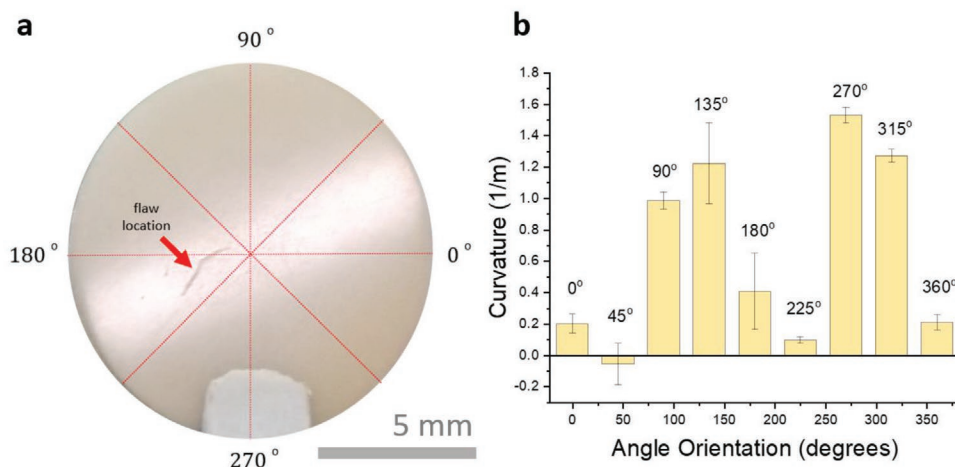


Figure 7. a) Visual representation of the laser orientation angles relative to the crack location after the experiment shown in Figure 6a. The data from Figure 6a were measured with the laser orientation angle of 0 degrees. b) Measured curvature values versus laser orientation angle after the experiment shown in Figure 6a. The curvature values were measured in 45 degrees increment relative to the original laser orientation (0 degrees). The figures clearly indicate that the orientations parallel to the flaw orientation (45 and 225 degrees) show the least amount of curvature change, while the orientations close to perpendicular to the flaw (135 and 315 degrees) exhibit the maximum.

however, during both OCV holds the curvature continues to increase, but at a slower rate. This is consistent with the observations in Figure 5 which show that steady-state stresses (fixed curvature) are only achieved after longer galvanostatic holds. In Figure 6 the experiment was halted before a short circuit occurred. In the post-mortem image, a significant flaw is visible on the plating side of the LLZO pellet. This flaw was then observed directly in the SEM, where a dark line is evident as shown in Figure 6d,e (this was not visible in the optical image). The features in Figures 6c–e were not observed on the separator side in Figure 6b. The cross-section image of the feature on the plating side was obtained by Focused Ion Beam (FIB) milling (see Figure 6f). Here, partial lithium metal penetration beneath the flaw is clearly shown and supported by the EDS map in Figure 6g. The oxygen signature here is interpreted as evidence of lithium metal, due to reaction between air and the plated lithium during the transfer to the SEM/FIB. It is unclear whether this flaw was initially created during the pellet synthesis process, however, this particular experiment provides an important opportunity to examine the cause of stress evolution.

In Figure 7 the surface flaw/feature's spatial orientation is correlated with the orientation that was used to track the curvature changes during the in situ measurement in Figure 6a. At the end of this experiment, additional curvature values were taken at different orientations by rotating the sample in 45 degrees increments. These data were collected with the reflected laser spots aligned along the red lines that are shown in Figure 7a. Here, the “0” degree orientation marked in Figure 7a corresponds to the orientation used in the in situ measurements. The results in Figure 7b exhibit significant anisotropy in the curvature at different orientations. Both sets of measurements (made at slightly different locations) indicate that the maximum curvature values correspond to the orientation that is roughly perpendicular to the surface flaw in Figure 6c. Although it is unclear how this feature was created, the data in Figure 7b show that it is closely correlated with the curvature measurements. This result strongly supports the

idea that Li metal penetration into this flaw leads to significant stress generation in the LLZO.

Asymmetric bending was also observed in seven other experiments where plating was halted before a full short-circuit occurred. Post-mortem SEM imaging revealed smaller dark lines indicative of Li penetration in some, but not all of these specimens. None of these other specimens showed the type of large flaw seen in Figures 6c and 7a, which confirms that this defect is probably associated with the more prominent dark line in Figure 6c. The lines that were discernible by SEM in other specimens were shorter and did not generally run close to the middle of the specimen (i.e., the one in Figure 6 is an exception). Thus it is difficult to assess the relationship between these penetration lines and the observed bending. However, the observation that asymmetric curvature occurred in all of these samples indicates that the stresses that develop here are not radially symmetric. For cases where smaller lines were observed, note that sample-to-sample variability is likely to occur because of the inherent challenges associated with the specimen preparation and because of the unknown penetration depth at the point where the experiment was terminated (i.e., some experiments may have been halted before there was enough penetration to produce identifiable lines, etc). Note here that the more obvious lithium penetration that was observed in the shorted samples (e.g., Figure 4b) was not seen in optical images of the specimens where plating was halted before a short (including the one in Figure 6). This suggests that initial lithium penetration is associated with thinner filaments and less lithium than that observed in specimens where shorting occurred (i.e., in Figure 4), although it is difficult to be sure of this (i.e., since these initial filaments were not directly imaged here).

2.4. Interfacial Reactions

Interface reactions are known to occur between the LLZO and both the Li metal and the liquid electrolyte (LE),^[38,42,43] and it is

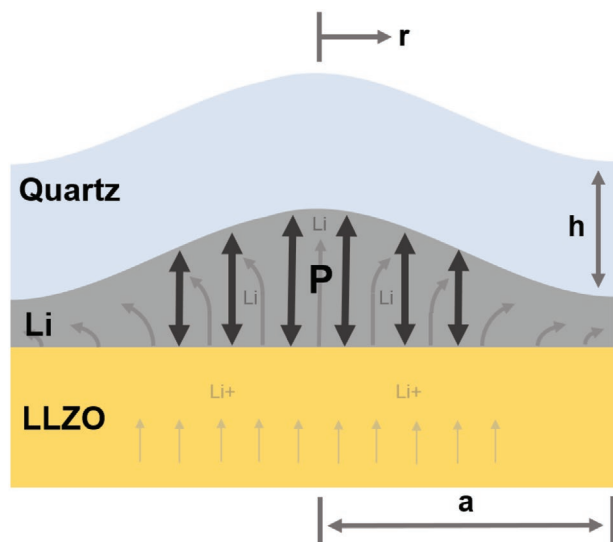


Figure 8. Schematic illustrating Li fluxes in the lithium metal layer during plating. During this process, the lithium metal redistribution homogenizes the internal pressure. The free surface at the edges leads to reduced upward pressure on the quartz (see Equation (1) and the related discussion).

possible that these surface layers are accompanied by stresses that contribute to the measured curvatures. The use of an ALD alumina layer minimizes both the chemical and mechanical contributions from reactions at the Li metal/LLZO interface.^[11,44,45] The effects of the reaction at the LE/LLZO interface were investigated directly with the experiments reported in Section IV, Supporting Information. The chemical analysis of these layers (Figure S7, Supporting Information) indicates that they are similar to those reported in the previous studies cited above. The slight decrease in curvature here suggests that there is a relatively small compressive stress at the LE/LLZO interface (the curvature magnitude here is <1% of the increases observed during plating). Increasing the current density to 0.01 mA cm⁻² after 200 h in Figure S8c, Supporting Information also results in a rapid increase in curvature. Thus, interface reactions are not the primary cause of the curvatures reported in Figures 4–7 and Figures S1,S2,S4, Supporting Information. Although the stresses induced by the interface reactions are large enough to have a relevant impact on phenomena occurring at the Li/SE interface, the overall measured curvature evolution is dominated by processes associated with lithium plating, as outlined above.

3. Analysis and Discussion

3.1. Relationships between Curvature and Stresses during Plating

Evaluation of the experiments focuses on interpreting the measured curvatures that evolve during electrochemical cycling. Wafer curvature is often used to obtain a value for the average in-plane biaxial stress in a thin film via analytical descriptions (e.g., Stoney equation, etc).^[46] However, the deformation of the

stack in Figure 3 is more complex and detailed analysis is thus required. In these experiments the measurements directly track bending of the inert quartz wafer, induced by internal stress changes in the underlying Li metal layer. During plating, the pressure that the lithium exerts on the quartz cause it to move upward, since this top wafer is not constrained. This pressure is equivalent to the hydrostatic stress at the quartz/lithium interface. The measured curvatures indicate clearly that pressure in the Li is not uniform (i.e., with uniform pressure the wafer would remain flat). In the experiments the upward force acting at the edges of the Li layer is reduced because the radial expansion of the Li is not confined here (i.e., because of the free surface on the side of the specimen). Due to this effect, the upward forces acting on the quartz wafer will be lower near the edges than they are at positions that are closer to the center. Forces acting on both the quartz and Li metal layers are shown schematically in Figure 8a. As shown here, shear forces acting at the Li/quartz interface will be significant near the edge. The size of this region, δR_{edge} , can be approximated with a simple shear lag analysis,^[47] which gives the following approximate scaling:

$$\delta R_{\text{edge}} \approx \frac{\sigma_{rr}}{(\tau_{\text{int}}^Q + \tau_{\text{int}}^{\text{SE}})} h_{\text{Li}} \quad (1)$$

The stress in the Li layer is limited by plasticity, such that $\sigma_{rr} \approx \sigma_{\text{Li}}^Y$. The interfacial shear resistance at the quartz and SE interfaces are then given by τ_{int}^Q and $\tau_{\text{int}}^{\text{SE}}$, respectively. In general, the interface behavior is limited by the frictional sliding strength of the interface or the shear flow stress of the lithium, whichever is smaller. The low yield stress of lithium suggests that this is the limiting factor here, such that $\tau_{\text{int}} \approx \sigma_{\text{Li}}^Y/2$.^[48] This gives $\delta R_{\text{edge}} \approx h_{\text{Li}}$, which then indicates that $\delta R_{\text{edge}} \ll R$ for the experimental configuration.

The basic shear lag treatment outlined above also indicates that the upward force on the quartz wafer is substantially reduced inside of the small edge region. This suggests that the steady-state curvature observed after longer plating times is associated with a lower upward pressure at the edges. With this in mind, an approximate estimate of the relationship between pressure and curvature was obtained from standard analysis of bending in circular plates with a supported edge. The resulting displacement normal to the plate and the curvature are then described by:^[49]

$$\frac{w(r)}{a} = \frac{3}{16} \frac{P}{E'} \left(\frac{a}{h} \right)^3 \left[1 - \left(\frac{r}{a} \right)^2 \right] \left[\frac{5+\nu}{1+\nu} - \left(\frac{r}{a} \right)^2 \right] \quad (2)$$

$$\kappa(r) = \frac{d^2 w}{dr^2} = \kappa_o \left[1 - \frac{3(1+\nu)}{(3+\nu)} \left(\frac{r}{a} \right)^2 \right] \quad (3)$$

where E' is the plane-strain Young's Modulus, $E/(1 - \nu^2)$, h is the thickness of the quartz wafer, P is the pressure applied normal to the wafer surface, and

$$\kappa_o = - \frac{3(3+\nu)}{4(1+\nu)} \frac{P}{E'} \frac{a^2}{h^3} \quad (4)$$

Table 1. Mechanistic explanations of curvature evolution during plating.

Observations	Proposed explanations
1. During initial plating, the curvature changes that occur are inconsistent (see Figures 4a, 5, 6a, and Figure S1, Supporting Information).	It is likely that the initial curvature response during Li plating varies because of inhomogeneities in the material. One issue is that non-uniform Li metal contact during sample fabrication will leave voids at the interface. This will lead to non-uniform redistribution of Li near the interface during initial plating, such that the initial pressure build-up in the Li layer is complex and unpredictable. The sintering process also inherently produces variations in the microstructure which can alter Li plating behavior within a given sample, and also from sample to sample. ^[30]
2. During galvanostatic holds with increasing current densities of several hours or more, the curvature increases sharply.	The curvature increase reflects pressure build up in the Li layer. Based on Equation (5), the magnitude of the curvature indicates that most the lithium is deforming elastically here. The onset of plasticity occurs relatively slowly because the total amount of plating over several hours at currents below 0.05 mA cm ⁻² is a relatively small fraction of the total amount of lithium present (i.e., with an initial estimated thickness of ≈ 100 μm).
3. The curvature increase ceases after much longer galvanostatic holds at current densities below the CCD.	This is consistent with large scale plastic deformation throughout the lithium layer, and steady-state conditions where plating continues to increase the amount of Li in the layer without further increases in the curvature. During steady-state the quartz wafer continues to move away from the LLZO during plating (i.e., where the relative out-of-plane displacements across the wafer are constant).
4. Increasing the current density increases the curvature.	The steady-state pressure corresponds to a balance between the Li flux into the Li layer during plating, along with upward motion of the quartz and some relaxation at the edges. The results then indicate that a higher flux into the lithium layer during plating alters the steady-state balance in a way that causes a modest increase in the pressure.
5. OCV holds: (a) prior to steady-state, curvature is maintained, and increases slightly in some cases (Figure 6a); (b) at steady-state, curvature decreases slightly (Figure 5a).	Prior to steady-state, the slight increases during OCV seen in some experiments are potentially consistent with the slow redistribution of lithium and the evolving stress field in the metal layer. At steady-state the slight decrease is consistent with limited stress relaxation at the edges, as described in item (4).

is the curvature at $r = 0$. Rearranging this gives an expression that makes it possible to estimate the pressure as a function of the curvature in the center of the plate:

$$P = -E' \frac{4(1+\nu)}{3(3+\nu)} \frac{h^3}{a^2} \kappa_0 \quad (5)$$

Using quantities on the right side for the experimental configuration (e.g., quartz glass wafers with $a = 5$ mm, $h = 0.5$ mm, $E' = 74.1$ GPa, and $\nu = 0.17$), a value of $\kappa_0 = 0.5$ m⁻¹ corresponds to P of 0.09 MPa. This is substantially larger than the force needed to move the quartz wafer upward during plating, which indicates that this kind of static analysis can provide an approximate interpretation of the curvature (i.e., where steady-state corresponds to a uniform upward velocity across the quartz wafer, and the zero displacement condition used at the boundary is justified). The supported edge solution is also based on a zero moment at the boundary. This is likely to be an oversimplification, because the quartz is attached to the lithium layer at the edge. Another standard limiting case is a fully clamped boundary, where the value of P for a given curvature is roughly four times higher than that obtained from Equation (5).^[49] It is likely that the actual behavior in the experiments falls in between these two limits (i.e., at the edge there is some resistance to bending from the underlying Li, but it is significantly less rigid than the clamped case). Because the Li is very soft, the result in Equation (5) is likely to be a better approximation, however, the actual value of P should be somewhat higher than this estimate.

It is also important to note that while the measurements were made in the middle of the specimens, the distance between reflected laser spots means that the value is not obtained exactly

at $r = 0$. However, based on Equation (3), $\kappa(r)$ shows only moderate variations with position near the center such that with the typical spacing (≈ 1.7 mm), equating κ_0 with the measured curvature values will underestimate P by less than 5%. In light of the complicating factors discussed above, the maximum steady-state curvature values reported in Figure 5 appear to correspond to $P \approx 0.1$ – 0.2 MPa. This is remarkably close to the reported bulk yield stress of Li metal. Based on this agreement, Equation (5) gives a reasonable lower bound estimate of the internal pressure in the lithium metal during plating. This approximate interpretation then provides a basis for interpreting the key experimental results that are listed in **Table 1**. Sample to sample variations in the initial curvature response (item 1) are likely to be affected by initial inhomogeneities at the Li metal/SE interface. The phenomena listed in items 2, 3, 4, and 5 are all highly reproducible. These occur after more Li has been plated, and they can be explained in terms of the processes that are shown schematically in Figure 8.

3.2. Short Circuit Events

The experimental results indicate that short circuits are correlated with abrupt changes in the curvature. In some cases there is a sharp drop (Figure S1b, Supporting Information), while in other cases the pressure increase stops abruptly (Figures 4, 5a, and Figure S1a, Supporting Information). In comparison with these short circuit events, the changes that occur during the OCV holds are less pronounced, and sharp drops like that in Figure S1b, Supporting Information were not observed. The relatively modest changes that occur during OCV holds are generally consistent with the mechanisms that are summarized in

Table 1. The more dramatic curvature changes that correspond to short circuits indicate that these events are correlated with relaxation of the pressure that builds up in the Li layer during plating. These sharp changes are consistent with the idea that the lithium penetration of the LLZO (observed in post-mortem images) is a fracture-like process.

The CCD values observed here are low compared to most solid-state cells employed in prior studies.^[50] The absence of any applied stack pressure in these in situ measurements almost certainly reduces the CCD. Here, it is important to recognize that these values reflect averages over the entire specimen. Since external stack pressure is expected to produce a more homogeneous current distribution that increases the measured CCD, it is not clear if the local current densities that feed a growing filament in our experiments are actually lower (at the very least, any differences are expected to be significantly smaller than the difference in the measured CCD values). The curvature plateaus observed after sufficiently long times indicate that in the absence of stack pressure, the lithium metal self-pressurizes. This suggests that higher pressures here should lead to a more homogeneous current distribution and a higher CCD. The results for the seven samples where shorting occurred were too scattered to test this hypothesis, however, this could be investigated with curvature measurements in a focused, more detailed investigation.

To understand the curvature responses after short-circuit events, note that the pressure in the Li metal layer pushes against both the quartz wafer and the underlying LLZO. It then follows that fracture of the underlying LLZO will reduce the way in which the stiff ceramic electrolyte constrains the thinner, softer Li metal layer. The measured curvature when the Li depressurizes will depend on the corresponding deformation of the Li layer (elastic and plastic), and also on the position of the fracture event (i.e., penetration line), relative to the laser spots that are used to measure curvature. These intertwined effects and the corresponding position dependences explain why the curvature change associated with the short circuits varies significantly from sample to sample. In general, one would expect simple brittle fracture of the LLZO to suddenly decrease the pressure in the Li layer, which is consistent with the sharp curvature drop in Figure S1b, Supporting Information. The flat response in Figure 4b is also potentially consistent with fracture of the LLZO, since the sharp increase in curvature that occurs immediately before the short circuit indicates that the pressure in the lithium metal is still building up in this experiment (i.e., it has not yet reached steady-state). For comparison, the results in Figure 6a show increasing curvature during OCV holds, which indicates that the relatively slow evolution of the stress field in the Li metal can lead to increasing curvature after the lithium flux into the layer has stopped (this is potentially consistent with slow relaxation due to creep near the edges of the Li layer). Here, it should also be noted that the abrupt curvature change that corresponds to the short circuit in Figure 4a is significantly sharper than any of the changes observed for OCV holds.

The observation that visible lines only appear in samples that short, combined with the abrupt change in curvature that occurs at the same time, supports the hypothesis that this is a fracture-like phenomenon. The SEM images in Figure 4c,d

provide information about the nature of this failure process. Previous work attributes these patterns to Li penetration along GBs, however, the observations in Figure 4 provide some additional insight, particularly when considered along with the observation that the appearance of these features is correlated with depressurization of the lithium metal. Several microstructural phenomena are potentially relevant to further interpretation of these images:

- If Li penetration is associated with GBs, it is unclear why this only occurs along certain boundaries. Here, it is important to recognize that the sintering process inherently leads to local variations in microstructure and composition, which can result in different GB structures and local composition differences from grain to GB. This is likely to alter Li plating behavior within a given sample, and also from sample to sample.^[30]
- Different GB structures within a given sample can potentially result in inhomogeneous local ionic conductivities,^[51] which could in turn lead to enhanced Li penetration along certain preferred GBs. Recent findings also provide evidence of enhanced electronic conductivity in some GB regions, which can promote localized reduction of Li^+ ^[35,52] (i.e., this is a specific example of a situation where not all grain-boundaries are created equal and lithium metal penetrates only through some GBs observed in Figure 4c,d).
- Preferred Li penetration along GBs implies that the ceramic regions between the Li lines will initially remain connected across the penetration line (i.e., such that the observed Li network forms around fully intact LLZO regions). However, this means that Li penetration will only lead to a small decrease in the stiffness of the material across the penetration line (i.e., roughly by the area fraction of Li). This in turn implies that the ability of the LLZO disk to support the pressure in the Li metal layer is only reduced slightly, which is not consistent with the depressurization in Figure 4b. An alternative explanation is that the LLZO regions in the images (visible between the Li lines) undergo fracture during Li penetration.^[30] This would require large local pressures in the Li metal inside of the LLZO (i.e., large enough to induce fracture).
- Another possibility is that Li penetration covers a larger area of the fracture surface in the image, but that the process of breaking the specimen after the experiment creates the pattern that is actually observed. Here, the soft Li metal is expected to undergo ductile rupture, such that the pattern observed in the images could occur when a thin Li layer stretches and forms ligaments between the two LLZO surfaces as the two electrolyte pieces are pulled apart. For this to fully explain the images, the exposed LLZO would have to fully dewet during this process (i.e., in light of the fact that the LLZO GBs are seen in the images).

Based on the experimental results, it is currently difficult to determine which of the factors described above are most important. While additional research is needed to investigate these effects in more detail, it is clear that Li penetration is impacted by the inhomogeneous nature of the polycrystalline LLZO.^[30] Also, in comparison with previous work, the network structures in Figure 4 provide unique information about variations that occur across the SE, due to the applied unidirectional current.

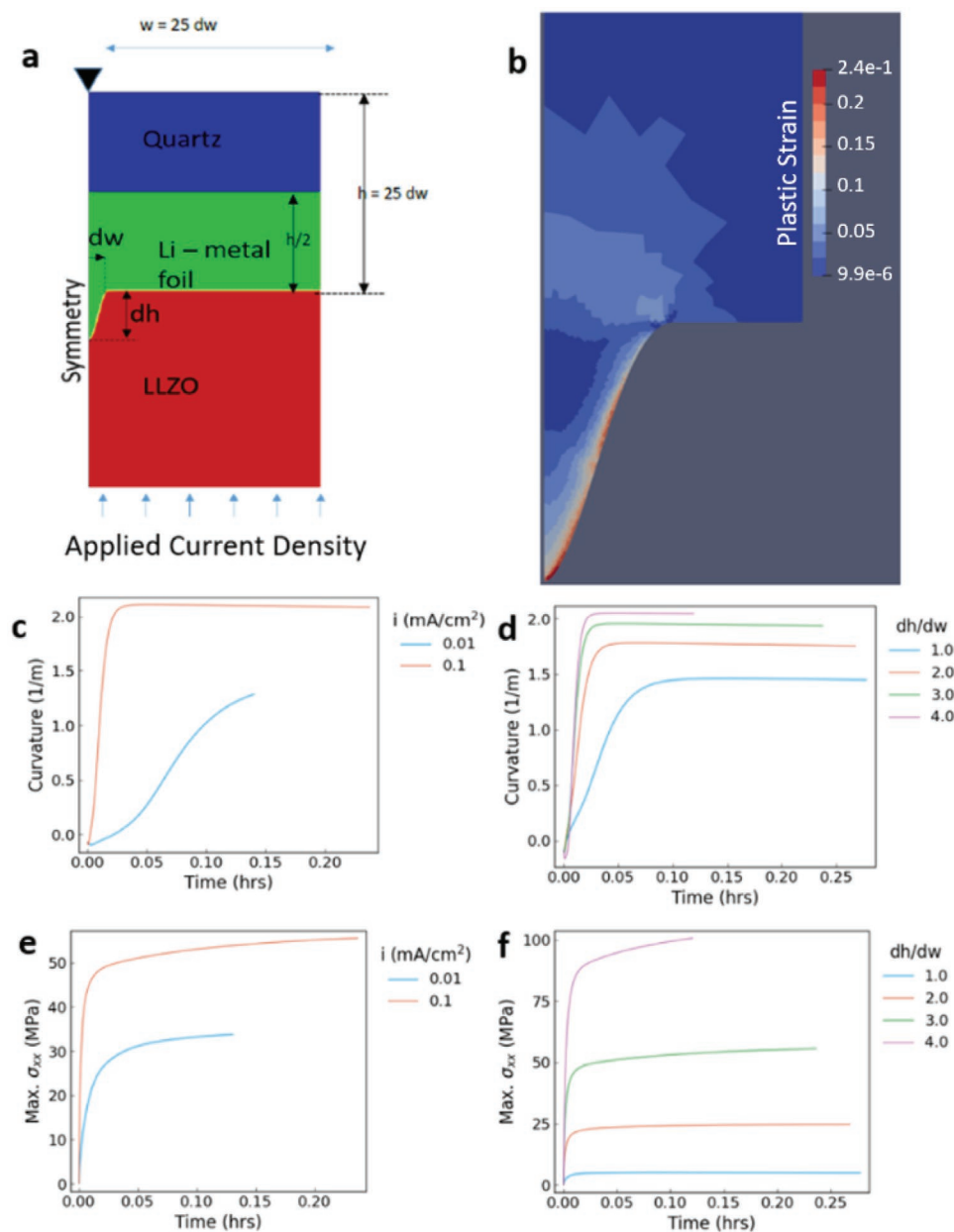


Figure 9. a) Configuration for FEM; b) evolution of plastic strain in the deposited Li and Li foil ($dw = 2.0 \mu\text{m}$, $dh = 4.0 \mu\text{m}$, and current density = 0.1 mA cm^{-2}); c,e) evolution of curvature and stress with current density ($dw = 2.0 \mu\text{m}$, $dh = 6.0 \mu\text{m}$, current density = 0.01 and 0.1 mA cm^{-2}); d,f) evolution of curvature and maximum stress as a function of aspect ratio ($dw = 2.0 \mu\text{m}$, $dh = 2.0, 4.0, 6.0, 8.0 \mu\text{m}$, current density = 0.1 mA cm^{-2}).

3.3. Asymmetric Bending

The analysis in Equations (1)–(5) and the subsequent discussion addresses circular samples where the boundary conditions and bending are radially symmetric. The observed asymmetric bending in Figure 7 indicates that additional factors must be considered. The position of the electrical contact at the side of the wafer (see Figures 3 and 7) does not appear to be correlated with the bending asymmetry in the experiments. Instead, the hypothesis that emerges from Figure 7 is that asymmetric bending is associated with the dominant Li-filled flaw. To assess this further, the detailed FEM in the Experimental Section considers plating

in the vicinity of a surface flaw, based on the configuration in Figure 9a. The dimensions of the flaw are similar to the one in Figure 7, and the plane strain analysis is also consistent with the experimental configuration (i.e., the length of the actual flaw is several orders of magnitude larger than its width and height). This model includes a full electrochemical description of Li plating and also evaluates mechanical deformation in both the LLZO and Li metal. Interfacial reactions with the liquid electrolyte are neglected, since the results in Figure S8, Supporting Information indicate that these make only a small contribution.

The electro-chemo-mechanics of plating in the vicinity of a flaw are illustrated in the results shown in Figure 9. For

the conditions that were examined, the Li deposition rate is significantly higher at the bottom of the flaw, when compared to the outside of the flaw. Since this system is free standing any morphology changes in the electrodeposited Li will result in a morphological change at the Li-metal/quartz glass surface. Fitting the calculated displacements to a smoothing spline made it possible to compute the curvature at each point. Figure 9c,d shows the resulting temporal evolution of curvature during plating. The deformation and curvature initially increase with time as more Li is deposited inside the flaw (compared to the deposition rate outside of the flaw). With continued plating, the Li deforms plastically due to the constraint of the ceramic flaw surface and the non-uniform local Li deposition rates. Finally, the morphology evolution reaches a steady state, balancing plastic deformation and non-uniform deposition, where the curvature remains constant in time. This trend closely matches the experimental observations (e.g., in Figure 5).

Another key observation is that the magnitudes of the curvature are similar to those in the experiments in Figures 4–7. Figure 9d shows the time evolution of curvature for $dw = 2.0 \mu\text{m}$, and different dh with a constant applied current density of 0.1 mA cm^{-2} (changing dh while keeping dw fixed changes the aspect ratio of the surface flaw). Based on the agreement between the FEM and the key experimental trends outlined above, we postulate that the asymmetric curvature in the experiments arises primarily from non-uniform plating and the associated morphological surface evolution of the electrodeposited Li. The simulation results show that this leads to large plastic strains in the Li metal in the vicinity of the flaw, as seen in Figure 9b. The evolution of this strain is directly related to the evolution of the curvature, such that the steady-state curvature is associated with a steady-state strain field. The dynamic nature of this process is reflected in the predicted relationship between the current density and the steady-state curvature in Figure 9c. Here, increasing the current leads to higher plastic strains in the vicinity of the flaw. As noted above (e.g., in Table 1), this impact of current density on the curvature was also observed in the experiments and not readily explained with the static analysis based on Equation (5).

The simulations also provide a detailed description of the stresses in the Li filled flaw during plating. Calculated values for the maximum stress in the LLZO, at the tip of the flaw are shown in Figure 9e,f. These results show stresses that can exceed the Li metal yield stress by more than two orders of magnitude. This is a direct result of the enhanced Li plating inside of the flaw. The stress build up here reflects a balance between the plating kinetics and the flow of lithium out of the flaw, where the latter is constrained by the deformation of the metal in the immediate vicinity. In principle, the predicted stresses in Figure 9 provide a basis for assessing fracture of the LLZO. It is important to recognize that these calculated values depend on the assumed geometry of the flaw tip. While the maximum values in Figure 9 exceed the reported LLZO fracture strength, they are localized and may not provide a sufficient driving for crack extension. However, with a Griffith-style sharp crack tip the stress concentration in the vicinity of the tip would be much larger. Figure 9f also shows that higher stresses will occur in deeper flaws. Another factor that may lead to fracture is that inside of a sufficiently narrow flaw, size scale effects are likely to increase the

lithium yield stress to values that are significantly higher than the bulk value that is used in the simulation. This will also lead to higher stresses in the LLZO and promote fracture.

Insight into other experimental observations was also obtained from the simulations. For example, the interpretations in Table 1 describe general redistribution of Li metal, without information about specific configurations. The simulation results in Figure 9 provide detailed information about this in the vicinity of a surface flaw. Also, in the initial measurements with shorter galvanostatic holds, the increasing curvature in the experiments corresponds to continuing evolution of the deformation field in the Li metal that resembles an overall elastic response in the lithium layer. While the simulation indicates that this is accurate for much of the layer, the FEM results show that the curvature response can also reflect the effects of localized current focusing near inhomogeneities.

4. Conclusions

There is currently an ongoing debate about the causes, form, and critical conditions for break down due to Li-metal penetration through solid state battery electrolyte materials. In the current presents a blueprint for using in situ curvature measurements as a novel approach to investigate chemo-mechanical phenomena during lithium plating through an LLZO SE. The results indicate that stress evolution in the lithium metal layer can be monitored during plating, and that the corresponding mechanical deformation reaches a steady-state after many hours. The measured pressure during plating, comparable to the Li yield stress, is dictated by several dynamic processes, including the Li flux through the electrolyte, the growth of the Li layer, and plasticity. The configuration used for these measurements differs from a realistic solid state battery. However, the general result that stress evolution in the Li metal electrode is a relatively slow process is likely to be broadly applicable to different cell designs. Another important observation is that short circuit events are directly correlated with a well-defined pressure change in the Li metal, indicative of a “fracture-like” event in the SE. The results also show that the increased lithium flux through surface flaws can lead to large localized plastic strains, and the corresponding simulation of this process predicts that large hydrostatic stresses can be created at the tip of surface flaws. Additionally, cross-sectional electron microscopy images of the short-circuit path show a web-like Li network with significant morphological variation between the plating and stripping side of the LLZO pellet. These observations suggest that Li metal penetration is affected by local inhomogeneities and chemical composition variations in the grain and/or GB localities of these sintered materials. More broadly, this study strongly suggests that these failure events originate from inherent defects in the LLZO SE, and that minimizing these defects during manufacturing is essential for a viable commercial product.

5. Experimental Section

LLZO Synthesis: $\text{Li}_{6.5}\text{La}_3\text{Zr}_{1.5}\text{Ta}_{0.5}\text{O}_{12}$ (LLZO:Ta) ceramics were prepared by solid-state synthesis based on the previous publication.^[53]

Table 2. Basic material properties and available variables.

Material	Description	E [Gpa]	ν	κ [mS cm ⁻¹]	Variables
Quartz	Elastic, no conduction	78	0.25	N/A	U _x , U _y
LLZO	Elastic, ionic conductor	170	0.3	0.1 (M ⁺)	U _x , U _y , Voltage
Li-metal foil*	Rate dependent elastic/plastic, electronic conductor	7.8	0.38	100 (e ⁻)	U _x , U _y , Voltage
Deposited Li metal*	Rate dependent elastic/plastic, with unidirectional swelling normal to interface	7.8	0.38	100 (e ⁻)	U _x , U _y , swelling, Voltage

Chemical formula was chosen due to their high bulk conductivity.^[54] A stoichiometric amount of La(OH)₃ (Sigma Aldrich, 99.9%), ZrO₂ (Sigma Aldrich, 99.9%), Ta₂O₅ (Sigma Aldrich, 99.99%), and 7 wt% excess LiOH (Alfa Aesar, purity 99.8%) were mixed by planetary milling (PM, Across International, PQ-N04) in absolute isopropanol using ZrO₂ balls for 1 h at 500 rpm. After drying the solvent, the powder compacts (pellets) were prepared, and the first calcination step was performed in MgO crucibles in a tubular furnace under constant flow of air at 800 °C for 10 h. Afterward, the pellets were crushed and subsequently grinded by PM for 12 h at 500 rpm. The grinded and dried powder was calcined at 800 °C in air for 5 h. For the final sintering step, powder compacts each around 0.5 gram were prepared using a pressing die/mold with a diameter of 12 mm and thickness of 1.5 mm in a uniaxial press. The green pellets were sintered in a MgO crucible under oxygen at 1100 °C for 5 h. The sintered LLZO pellets were dry-polished down to ≈700–900 nm to maintain a consistent surface finish among all the samples.

Sample Preparation of Reflective LLZO/Quartz Electrode: Each specimen was prepared by bonding a reflective quartz glass wafer (double-side polished, 500 μm thick, 1 cm diameter) and the LLZO pallet (500 μm thick, 1 cm diameter) together with a thin layer of molten lithium metal (≈100 μm thick). The quartz wafers were highly reflective after deposition of a multilayer current collector film consisting of 15 nm Ti, followed by a 200 nm Cu film, and a top layer of 50 nm Au. These were deposited via electron-beam evaporation at rates of 0.7, 1.2, and 1 Å s⁻¹, respectively. This current-collector on quartz wafer confines lithium metal during plating and minimizes roughening of the current collector (see discussion of Figure 2). Each LLZO pellet was annealed at 350 °C (under Argon flow for 5 h) and polished with a silicon carbide polishing paper up to 7000 grit to remove the residual carbonate layer. Atomic Layer Deposition (ALD) of 5 nm thick alumina (Al₂O₃) was then used to create a lithophilic layer on a single side of the pellet. Trimethyl aluminum (TMA, Sigma Aldrich, USA) and high performance liquid chromatography (HPLC) grade water (Sigma Aldrich, USA) were used as precursors in the ALD system (Cambridge Nanotech). The surface of the lithium metal was first scratched until appeared shiny, then was placed on top of the ALD-deposited side of the LLZO pallet with a hot plate underneath at 200 °C, above lithium metal's melting temperature. The current collector side of the quartz was placed directly on top of the molten lithium, with a thin strip of Cu foil placed in between for electrical contact. A small amount of pressure was then applied to fully bond the reflective quartz and the LLZO pellet together (see Figure 3a).

Curvature Measurement: Multi-beam Optical Sensor (MOS) measurements were conducted in custom-made electrochemical cells that permit optical access, using Li foil as the counter electrode.^[55] This technique measures wafer curvature changes during electrochemical cycling, by monitoring the spacing between reflected laser beams (see Figure 1b). Because the electrodes were essentially free-standing, 10 μL of 0.4 M LiNO₃ 0.6 M LiTFSI in DOL:DME (1:1) liquid electrolyte and a separator (Celgard) were placed in between LLZO and the counter Li foil electrode to ensure optimal contact during bending of the specimen. After the experiment, additional curvature measurements were carried out for some samples to evaluate anisotropic curvatures at different orientation angles. During each measurement, the cell was rotated at 45 degrees clockwise until the sample has been rotated completely.

Electrochemical Methods: Galvanostatic plating tests were performed with a Bio-Logic VSP potentiostat at 0.01 mA cm⁻², followed by stepwise

increases in the current density with 0.01 mA cm⁻² increments every 4–12 h. Some measurements included 10–12 h of OCV hold in between. Stripping was not included in this study to ensure one-directional plating and easily identify features that were relevant to the curvature evolution. EIS measurements were conducted from 1 mHz to 1 MHz before and after plating (only for the un-shorted samples). Similar EIS measurements were conducted with assembled cell sitting at OCV for every 24 h to distinguish contributions from liquid electrolyte reaction with LLZO. All measurements were conducted in room temperature conditions.

Post-Mortem Imaging: After the experiment, the cell was taken apart in an Argon-filled glovebox. A thin razor blade was used to slice and separate the LLZO pallet and the lithium metal. The LLZO pallet was then lightly polished to remove the residual lithium metal. After examining the surface, the crack created during cycling was examined with Scanning Electron Microscopy (FIB, FEI HELIOS 600) by either mechanically breaking the pallet along the crack or Focused Ion Beam milling. The cross-section of the crack was characterized by EDS mapping function.

FEM: In general, variations in the current and stress distribution at the Li metal-SE interface (due to geometric irregularity or material inhomogeneity) will lead to uneven Li electrodeposition. To evaluate the impact this has on the measured curvature a FEM was implemented with the Multiphysics Object-Oriented Simulation Environment (MOOSE). The simplified analysis used here treats a single surface feature that dominates the nonuniform morphology of plated Li. To this end, Li electrodeposition inside of a sinusoidal surface flaw parametrized with width dw and height dh was considered. A 25 dw wide section of the Li/SE system as shown in Figure 8a was then considered. The geometry was assumed to be axis-symmetric with symmetry axis at $r = 0$. The ceramic electrolyte was represented by a 25 dh thick layer which was modeled using classical small-strain formulation for an isotropic linear elastic material with $E = 170$ GPa and $\nu = 0.25$. The electrolyte was assumed to be a single-ion conductor with a conductivity $\kappa = 0.1$ mS cm⁻¹ (representative of LLZO^[54]). A 0.1 μm thick “interphase” growth layer was sandwiched between a Li metal layer with an average height of 12.5 dh . The interphase and the Li metal layer were modeled as an elasto-viscoplastic material with properties described in Table 2.^[56,57] In addition, the interphase layer was capable of unidirectional growth perpendicular to the electrolyte-interface. The “interphase” layer and the Li metal foil were assumed to be electronically conductive with $\kappa = 100$ mS cm⁻¹. Electro-chemical reactions were assumed to occur only at the SE/interphase layer interface and modeled with a charge transfer reaction described by linear Butler-Volmer kinetics. For the current results, these kinetics were described by a single charge-transfer-resistance $R_{ct} = 100 \Omega \cdot \text{cm}^2$ and assumed to be uniform across the entire SE/interphase interface. The electrochemical conditions at this interface were also coupled with a model of ionic conduction through the SE.^[58] Mechanical contact between the SE and interphase was modeled with lower-dimensional mortar elements and the displacements in all dimensions were set to be equal across the interface, mimicking perfectly bonded contact. Along the symmetry line, displacements were assumed to be zero in the radial direction and free in the z direction. A uniform current density was applied to the bottom of the electrolyte layer and the electric potential of the top surface of the Li-foil was set equal to zero.

Supporting Information

Supporting Information is available from the Wiley Online Library or from the author.

Acknowledgements

The work at Brown was primarily supported by the Department of Energy, Office of Energy Efficiency and Renewable Energy (EERE), under Award Number DE-EE0008863. Additional support from Samsung and discussions with Lincoln Miara (Samsung) are also gratefully acknowledged.

Conflict of Interest

The authors declare no conflict of interest.

Author Contributions

J.H.C., K.K., S.C., J.L.M.R., and B.W.S. discussed the design of the experiments. J.H.C. designed the in situ cell and conducted all relevant experiments. K.K. and J.L.M.R. fabricated and provided in-house LLZO solid electrolyte pallets for the experiments. S.C. carried out the simulation work. J.H.C., K.K., S.C., J.L.M.R., and B.W.S. contributed in writing the paper.

Data Availability Statement

The data that support the findings of this study are available from the corresponding author upon reasonable request.

Keywords

electro-chemo mechanics, Li metal, solid electrolytes

Received: January 29, 2022

Revised: March 8, 2022

Published online:

- [1] K. J. Kim, M. Balaish, M. Wadaguchi, L. Kong, J. L. M. Rupp, *Adv. Energy Mater.* **2021**, *11*, 2002689.
- [2] Y. Ren, Y. Shen, Y. Lin, C.-W. Nan, *Electrochem. Commun.* **2015**, *57*, 27.
- [3] E. J. Cheng, A. Sharafi, J. Sakamoto, *Electrochim. Acta* **2017**, *223*, 85.
- [4] M. Klinsmann, F. E. Hildebrand, M. Ganser, R. M. McMeeking, *J. Power Sources* **2019**, *442*, 227226.
- [5] L. Porz, T. Swamy, B. W. Sheldon, D. Rettenwander, T. Frömling, H. L. Thaman, S. Berendts, R. Uecker, W. C. Carter, Y.-M. Chiang, *Adv. Energy Mater.* **2017**, *7*, 1701003.
- [6] B. Kinzer, A. L. Davis, T. Krauskopf, H. Hartmann, W. S. LePage, E. Kazyak, J. Janek, N. P. Dasgupta, J. Sakamoto, *Matter* **2021**, *4*, 1947.
- [7] T. Swamy, R. Park, B. W. Sheldon, D. Rettenwander, L. Porz, S. Berendts, R. Uecker, W. C. Carter, Y.-M. Chiang, *J. Electrochem. Soc.* **2018**, *165*, A3648.
- [8] E. Kazyak, R. Garcia-Mendez, W. S. LePage, A. Sharafi, A. L. Davis, A. J. Sanchez, K.-H. Chen, C. Haslam, J. Sakamoto, N. P. Dasgupta, *Matter* **2020**, *2*, 1025.
- [9] B. Wu, S. Wang, J. Lochala, D. Desrochers, B. Liu, W. Zhang, J. Yang, J. Xiao, *Energy Environ. Sci.* **2018**, *11*, 1803.
- [10] C.-L. Tsai, V. Roddatis, C. V. Chandran, Q. Ma, S. Uhlenbruck, M. Bram, P. Heitjans, O. Guillon, *ACS Appl. Mater. Interfaces* **2016**, *8*, 10617.
- [11] X. Han, Y. Gong, K. Fu, X. He, G. T. Hitz, J. Dai, A. Pearse, B. Liu, H. Wang, G. Rubloff, Y. Mo, V. Thangadurai, E. D. Wachsman, L. Hu, *Nat. Mater.* **2017**, *16*, 572.
- [12] W. Luo, Y. Gong, Y. Zhu, Y. Li, Y. Yao, Y. Zhang, K. Fu, G. Pastel, C.-F. Lin, Y. Mo, E. D. Wachsman, L. Hu, *Adv. Mater.* **2017**, *29*, 1606042.
- [13] W. Luo, Y. Gong, Y. Zhu, K. K. Fu, J. Dai, S. D. Lacey, C. Wang, B. Liu, X. Han, Y. Mo, E. D. Wachsman, L. Hu, *J. Am. Chem. Soc.* **2016**, *138*, 12258.
- [14] C. Wang, Y. Gong, B. Liu, K. Fu, Y. Yao, E. Hitz, Y. Li, J. Dai, S. Xu, W. Luo, E. D. Wachsman, L. Hu, *Nano Lett.* **2017**, *17*, 565.
- [15] F. M. Pesci, R. H. Brugge, A. K. O. Hekselman, A. Cavallaro, R. J. Chater, A. Aguiar, *J. Mater. Chem. A* **2018**, *6*, 19817.
- [16] J. A. Lewis, J. Tippens, F. J. Q. Cortes, M. T. McDowell, *Trends Chem.* **2019**, *1*, 845.
- [17] Z. Shen, W. Zhang, G. Zhu, Y. Huang, Q. Feng, Y. Lu, *Small Methods* **2020**, *4*, 1900592.
- [18] W. S. LePage, Y. Chen, E. Kazyak, K.-H. Chen, A. J. Sanchez, A. Poli, E. M. Arruda, M. D. Thouless, N. P. Dasgupta, *J. Electrochem. Soc.* **2019**, *166*, A89.
- [19] W. Zhang, D. Schröder, T. Arlt, I. Manke, R. Koerver, R. Pinedo, D. A. Weber, J. Sann, W. G. Zeier, J. Janek, *J. Mater. Chem. A* **2017**, *5*, 9929.
- [20] M. Balaish, J. C. Gonzalez-Rosillo, K. J. Kim, Y. Zhu, Z. D. Hood, J. L. M. Rupp, *Nat. Energy* **2021**, *6*, 227.
- [21] S. Y. Han, C. Lee, J. A. Lewis, D. Yeh, Y. Liu, H.-W. Lee, M. T. McDowell, *Joule* **2021**, *5*, 2450.
- [22] T. Krauskopf, F. H. Richter, W. G. Zeier, J. Janek, *Chem. Rev.* **2020**, *120*, 7745.
- [23] B. S. Vishnugopi, E. Kazyak, J. A. Lewis, J. Nanda, M. T. McDowell, N. P. Dasgupta, P. P. Mukherjee, *ACS Energy Lett.* **2021**, *6*, 3734.
- [24] G. Bucci, T. Swamy, Y.-M. Chiang, W. C. Carter, *J. Mater. Chem. A* **2017**, *5*, 19422.
- [25] P. Barai, K. Higa, A. T. Ngo, L. A. Curtiss, V. Srinivasan, *J. Electrochem. Soc.* **2019**, *166*, A1752.
- [26] L. Barroso-Luque, Q. Tu, G. Ceder, *J. Electrochem. Soc.* **2020**, *167*, 020534.
- [27] C. Yuan, X. Gao, Y. Jia, W. Zhang, Q. Wu, J. Xu, *Nano Energy* **2021**, *86*, 106057.
- [28] G. Bucci, J. Christensen, *J. Power Sources* **2019**, *441*, 227186.
- [29] P. Barai, A. T. Ngo, B. Narayanan, K. Higa, L. A. Curtiss, V. Srinivasan, *J. Electrochem. Soc.* **2020**, *167*, 100537.
- [30] B. S. Vishnugopi, M. B. Dixit, F. Hao, B. Shyam, J. B. Cook, K. B. Hatzell, P. P. Mukherjee, *Adv. Energy Mater.* **2022**, *12*, 2102825.
- [31] C. D. Fincher, D. Ojeda, Y. Zhang, G. M. Pharr, M. Pharr, *Acta Mater.* **2020**, *186*, 215.
- [32] J. H. Cho, X. Xiao, K. Guo, Y. Liu, H. Gao, B. W. Sheldon, *Energy Storage Mater.* **2020**, *24*, 281.
- [33] Z. Ning, D. S. Jolly, G. Li, R. De Meyere, S. D. Pu, Y. Chen, J. Kasemchainan, J. Ihli, C. Gong, B. Liu, D. L. R. Melvin, A. Bonnin, O. Magdysyuk, P. Adamson, G. O. Hartley, C. W. Monroe, T. J. Marrow, P. G. Bruce, *Nat. Mater.* **2021**, *20*, 1121.
- [34] J. Tippens, J. C. Miers, A. Afshar, J. A. Lewis, F. J. Q. Cortes, H. Qiao, T. S. Marchese, C. V. Di Leo, C. Saldana, M. T. McDowell, *ACS Energy Lett.* **2019**, *4*, 1475.
- [35] F. Han, A. S. Westover, J. Yue, X. Fan, F. Wang, M. Chi, D. N. Leonard, N. J. Dudney, H. Wang, C. Wang, *Nat. Energy* **2019**, *4*, 187.
- [36] Q. Li, T. Yi, X. Wang, H. Pan, B. Quan, T. Liang, X. Guo, X. Yu, H. Wang, X. Huang, L. Chen, H. Li, *Nano Energy* **2019**, *63*, 103895.

- [37] I. k-Space Associates Inc., *kSA MOS Product Specifications*. k-space.com **2015**.
- [38] A. Sharafi, H. M. Meyer, J. Nanda, J. Wolfenstine, J. Sakamoto, *J. Power Sources* **2016**, *302*, 135.
- [39] F. Flatscher, M. Philipp, S. Ganschow, H. M. R. Wilkening, D. Rettenwander, *J. Mater. Chem. A* **2020**, *8*, 15782.
- [40] Y. Tian, F. Ding, H. Zhong, C. Liu, Y.-B. He, J. Liu, X. Liu, Q. Xu, *Energy Storage Mater.* **2018**, *14*, 49.
- [41] T. Dussart, N. Rividi, M. Fialin, G. Toussaint, P. Stevens, C. Laberty-Robert, *J. Electrochem. Soc.* **2021**, *168*, 120550.
- [42] M. Naguib, A. Sharafi, E. C. Self, H. M. Meyer, J. Sakamoto, J. Nanda, *ACS Appl. Mater. Interfaces* **2019**, *11*, 42042.
- [43] C. Ma, Y. Cheng, K. Yin, J. Luo, A. Sharafi, J. Sakamoto, J. Li, K. L. More, N. J. Dudney, M. Chi, *Nano Lett.* **2016**, *16*, 7030.
- [44] F. Deng, Y. Wu, W. Tang, S. Song, Z. Wen, M. Kotobuki, L. Lu, J. Yao, N. Hu, J. Molenda, *Solid State Ionics* **2019**, *342*, 115063.
- [45] K. Hofstetter, A. J. Samson, J. Dai, J. E. Gritton, L. Hu, E. D. Wachsman, V. Thangadurai, *J. Electrochem. Soc.* **2019**, *166*, A1844.
- [46] L. B. Freund, S. Suresh, *Thin Film Materials: Stress, Defect Formation and Surface Evolution*, Cambridge University Press, Cambridge **2004**.
- [47] S. K. Soni, B. W. Sheldon, X. Xiao, M. W. Verbrugge, A. Dongjoon, H. Haftbaradaran, G. Huajian, *J. Electrochem. Soc.* **2011**, *159*, A38.
- [48] R. v. Mises, *Nachr. Ges. Wiss. Goettingen, Math.-Phys. Kl.* **1913**, *1913*, 582.
- [49] S. Timoshenko, *Theory of Plates and Shells*, McGraw Hill, New York **1959**.
- [50] Y. Lu, C.-Z. Zhao, H. Yuan, X.-B. Cheng, J.-Q. Huang, Q. Zhang, *Adv. Funct. Mater.* **2021**, *31*, 2009925.
- [51] S. Smetaczek, A. Wachter-Welzl, R. Wagner, D. Rettenwander, G. Amthauer, L. Andrejs, S. Taibl, A. Limbeck, J. Fleig, *J. Mater. Chem. A* **2019**, *7*, 6818.
- [52] X. Liu, R. Garcia-Mendez, A. R. Lupini, Y. Cheng, Z. D. Hood, F. Han, A. Sharafi, J. C. Idrobo, N. J. Dudney, C. Wang, C. Ma, J. Sakamoto, M. Chi, *Nat. Mater.* **2021**, *20*, 1485.
- [53] K. J. Kim, J. L. M. Rupp, *Energy Environ. Sci.* **2020**, *13*, 4930.
- [54] Y. Li, J.-T. Han, C.-A. Wang, H. Xie, J. B. Goodenough, *J. Mater. Chem.* **2012**, *22*, 15357.
- [55] A. Mukhopadhyay, A. Tokranov, K. Sena, X. Xiao, B. W. Sheldon, *Carbon* **2011**, *49*, 2742.
- [56] L. Anand, S. Narayan, *J. Electrochem. Soc.* **2019**, *166*, A1092.
- [57] S. Narayan, L. Anand, *Extreme Mech. Lett.* **2018**, *24*, 21.
- [58] Q. Tu, T. Shi, S. Chakravarthy, G. Ceder, *Matter* **2021**, *4*, 3248.